

# Implications of mountain shading on calculating energy for snowmelt using unstructured triangular meshes

Christopher B. Marsh<sup>1,2</sup>, John W. Pomeroy<sup>1</sup> and Raymond J. Spiteri<sup>2,1</sup>

<sup>1</sup>Centre for Hydrology, University of Saskatchewan, Saskatoon, Canada S7N 5C8

<sup>2</sup>Numerical Simulation Laboratory, Dept. Computer Science, University of Saskatchewan, Saskatoon, Canada S7N 5C9

March 13, 2012

## Abstract

In many parts of the world, snowmelt energetics are dominated by solar irradiance. This is particularly the case in the Canadian Rocky Mountains, where clear skies dominate the winter and spring. In mountains, solar irradiance at the snow surface is not only affected by solar angles, atmospheric transmittance, and the slope and aspect of immediate topography but also by shadows from surrounding terrain. Accumulation of errors in estimating solar irradiation can lead to significant errors in calculating the timing and rate of snowmelt due to the seasonal storage of internal energy in the snowpack. Gridded methods, which are often used to estimate solar irradiance in complex terrain, work best with high-resolution digital elevation models (DEMs), such as those produced using LiDAR. However, such methods also introduce errors due to the rigid nature of the mesh as well as limiting the ability to represent basin characteristics. Unstructured triangular meshes are more efficient in their use of DEM data than fixed grids when producing solar irradiance information for spatially distributed snowmelt calculations and they do not suffer from the artefact problems of a gridded DEM. This paper demonstrates the increased accuracy of using a horizon-shading algorithm model with an unstructured mesh versus standard self-shading algorithms. A systematic over-prediction in irradiance is observed when only self-shadows are considered. The modelled results are diagnosed by comparison to measurements of mountain shadows by time-lapse digital cameras and solar irradiance by a network of radiometers in Marmot Creek Research Basin, Alberta, Canada. Results show that depending on the depth and aspect of the snowpack of the Mt. Allan cirque, 6.0% to 66.4% of the pre-melt

snowpack could be prematurely melted. On average at a basin scale there was a 14.4 mm SWE difference in equivalent melt energy between the two shading algorithms with maximum differences over 100% of the total annual snowfall.

Keywords: snowmelt, solar radiation, shading, mountains, triangulated irregular networks, unstructured mesh, radiation modelling, Canadian Rockies

## 1 Introduction

Shortwave radiation is emitted from the sun in the wavelengths of  $0.1 \mu\text{m}$  to  $4 \mu\text{m}$  (Petty, 2006; Wallace and Hobbs, 2006). Incident to the top of the Earth's atmosphere, the sun's incoming rays provide a flux of energy, termed the solar constant, of approximately  $1367\text{--}1368 \text{ W m}^{-2}$  (Willson, 2003). As this energy is transmitted through the atmosphere, the total flux of energy is reduced due to absorption and reflectance by atmospheric particulates and aerosols. On a flat plane, the radiation incident to the ground is comprised of diffuse- and direct-beam components. Diffuse irradiance is defined as the energy flux produced by a solar photon that has had one or more interactions with any atmospheric constituent, and direct irradiance is that produced a solar photon that has not interacted with any atmospheric constituent (Marshak and Davis, 2005). In any complex terrain there is a third component: reflected direct/diffuse irradiance from nearby terrain.

Shortwave radiation to the Earth's surface provides the driving force for many atmospheric, hydrological, and biological processes (Dymond, 2002; Oliphant et al., 2003; Ranzi and Rosso, 1995; Varley et al., 1996). One of the major hydrological processes impacted by shortwave radiation is snowmelt runoff (e.g., Male and Granger (1981)). Snowmelt often results in the largest discharge of the year; it transports contaminants that accumulated during the winter and recharges soil moisture reserves (Davies et al., 1987; Gray et al., 2001; Gray and Male, 1981). The seasonal melt of snow cover provides water for streamflow that can affect ecosystems far downstream from the source snowpack (Groisman and Davies, 2001). For instance, many western and northern North American rivers derive the majority of their flow from late spring snowpacks in the mountains and that then flows to low-lying regions (Stewart, 2009; Woo et al., 2008).

In mountainous areas with complex topography, snowmelt calculations are further complicated due to high spatial variability of energy fluxes (e.g., Marks and Dozier (1992); Pomeroy et al. (2003)). Slope and aspect have been identified throughout the literature as large contributors to the spatial variability of the surface energy balance, causing significant differences in snowmelt timing and magnitude (Carey and Woo, 1998; Dozier et al., 1981; Hopkinson et al., 2011; Pomeroy et al., 2003; Ryerson, 1984). A common situation is to have areas that are obscured from direct-beam irradiance because they are below the local horizon (i.e., are shaded by surrounding topography). These shadows are frequently referred to as *horizon-shadows* (e.g., Essery and Marks (2007)). Self-shadows form a subset of horizon-shadows that occur when a slope faces

away from the sun. In this case, the self-shadow is cast by the terrain only onto itself. These two shadow types lead to terrain cycling in and out of shadow, creating large differences in incident shortwave radiation and thus the surface energy balance. Horizon-shadows can play a principal role in limiting melt on glaciers that are nested in highly shaded cirques (*Chueca and Julián, 2004*), on snow melt (*Carey and Woo, 1998; Pomeroy et al., 2003*), in surface temperature (*Pomeroy et al., 2003*), and on photosynthesis and subsequent vegetation patterns (*Dymond, 2002*). In fact, much of the spatial variability in snowmelt energetics can be attributed to topographic influences (*Woo and Young, 2004*). This spatial variability of topographically driven irradiance is important in even gently rolling terrain as shown by *Pohl et al. (2006)* in a sub-arctic tundra river basin. Incorporating the effects of topography on solar irradiance is thus required for any of the processes dependent upon it, such as snowmelt. Failure to account for even basic features such as slope and aspect has been shown to be detrimental to snowmelt and stream flow prediction (*Dornes et al., 2008*). In modelling a sub-arctic catchment, *Davison et al. (2006)* concluded that incorporating surface slope and aspect is required for proper snow-cover ablation and runoff timing. *Pohl et al. (2006)* identified that the small-scale variability in solar radiation for the melt period is an important contributing factor for the development of patchy snow cover in the tundra and that it also controlled the timing and magnitude of melt water release to the basin. Fundamentally, correct surface irradiance prediction is a principal contributor of realistic snowmelt models (*Munro and Young, 1982*).

When considering an irradiance model that incorporates surrounding topographic features, the most common approach is the hemisphere viewshed/horizon calculation. Examples of horizon-based algorithms are those of *Fu and Rich (1999)* that are incorporated into the ArcGIS product by Environmental Systems Research Institute (ESRI) under the name SolarAnalyst, as well as those of *Dozier et al. (1981)*, *Dozier and Frew (1990)*, *Frew (1990)*, and *Varley et al. (1996)*. The general algorithm used in these studies can be described as follows. A structured gridded mesh (generally referred to as a raster or grid), rectangular in shape with a fixed spatial cell scale, is taken to define the topography. Then for each point in this mesh, the algorithm computes an upward-looking hemispherical viewshed by looking in all cardinal directions from a focal point and then determining the maximum elevation angle of the obscuring terrain (*Hetrick et al., 1993*). A continuous horizon is created by interpolating between the sampled horizon points. The horizon may be calculated many ways, such as via ray-tracing (*Coquillart and Gangnet, 1984*) or a sector/hull approach (*Stewart, 1998*). To determine if terrain is shaded, the horizon in the direction of the sun's azimuth is compared to the solar elevation and the terrain is shaded accordingly. One of the major difficulties with this type of algorithm is choosing a proper interval between sampling points when looking up and computing the horizon. Increasingly, high-resolution datasets are becoming available, and this necessitates a need for high-performance algorithms (*Tabik et al., 2011*) because more terrain elements must be checked. *Romero et al. (2008)* identified the horizon calculation and subsequent look-up in most shadow-aware models

as the most computationally expensive part of the irradiance calculation. There have been many attempts at producing increasingly efficient algorithms for the horizon calculation. A review of these methods can be found in *Tabik et al.* (2011).

Raster-based hydrological models are common because a raster’s computer representation can be implemented trivially using two-dimensional arrays, a feature intrinsic to any modern programming language. Despite their widespread use, rasters have a number of important limitations when used for hydrological modelling. For example, drainage directions and surface flow are constrained to  $45^\circ$  intervals, and geometric artefacts and variability can be artificially introduced because of the rigid structure (*Tucker, 2001*). In contrast to these structured grids, unstructured meshes have a number of advantages in hydrologic modelling. For example, because of the non-uniform spacing of points of an unstructured mesh, meandering features such as streams can be easily represented (*Tucker, 2001*). When river channel evolution was simulated by *Braun and Sambridge* (1997), the artificial constraints from using a raster were identified as the cause of creating non-natural channels. This was in contrast to the output from unstructured meshes that produced more natural-looking channels. *Tucker* (2001) suggested that unstructured meshes devised using triangulated irregular networks (TINs) should be preferred over raster DEMs. Unstructured meshes can provide a high-quality representation of the terrain using many fewer elements while maintaining conformance to the geometrical and physical properties of the basin (*Kumar et al., 2009*) to some predefined tolerance. Furthermore, landforms and associated topography need not be represented at the constant spatial resolution of a raster DEM, a resolution that generally corresponds to the highest resolution required to represent one area of the domain of interest (*Tucker, 2001*). *Tachikawa et al.* (1994) went as far to say that structured meshes are not appropriate for hydrological models due to their crude movement of water to only the eight adjacent cells (following the commonly used D8 routing method (*O’Callaghan and Marks, 1984*)). Because of the reduction in spatial information needed to properly quantify the basin due to a more efficient terrain representation (*Shewchuk, 1996*), *Ivanov et al.* (2004) found that for unstructured meshes there was a 5%–10% reduction in elements. When representing a non-rectangular hydrological basin, structured meshes necessitate buffering around the basin in order to capture its irregular shape with regular cells. This can result in having to either mask areas out, computing values for areas not being used in the simulation, or focusing on a ‘window’ within the basin that can be fully captured via a square/rectangular raster and neglecting the rest of the basin. However, unstructured mesh data structures are more complex than those for structured grids and the variable triangle sizes can place new requirements on algorithms. Although it is possible to utilize structured mesh algorithms with unstructured meshes, there are increasing complexities associated with this and the adaption of the algorithm to unstructured meshes may be prohibitively costly depending on the algorithm chosen.

This paper demonstrates the importance of capturing horizon-shadows when

modelling energy for snowmelt by using a modification of the *Montero et al.* (2009) algorithm. Because of the advantages of using an unstructured mesh for hydrological modelling, an unstructured mesh terrain discretization approach is used. We demonstrate that a failure to account for horizon-shadows results in a large cumulative difference in simulated energy compared to using only a self-shading algorithm. The difference between the self-shading and horizon-shading algorithms can cause significant errors in snow melt modelling and that late spring/summer snow packs could be partly accounted for by including horizon-shading.

## 2 Study site and methodology

The research was carried out over the winter of 2010 and the spring of 2011 at the Marmot Creek Research Basin (MCRB) 50.96° N and 115.21° W in the Kananaskis River Valley of the Canadian Rocky Mountains (Figure 1). The MCRB is operated by the Centre for Hydrology, University of Saskatchewan, and was initially established in 1962 by the Canadian Government as an experimental basin (*Golding, 1970*). A brief description of the MCRB follows.

The MCRB ranges in elevation from approximately 1450 m.a.s.l to 2886 m.a.s.l. At lower elevations, landcover is generally dense lodgepole pine, Douglas spruce, and subalpine fir; tree-line elevations are characterized by larch, spruce, fir, shrubs, and grasses; high alpine zones consists of talus and bare rocks (*DeBeer and Pomeroy, 2009; MacDonald et al., 2010*). The climatic conditions are dominated by continental air masses where winters are long and cold, averaging -15°C between January and March (*DeBeer and Pomeroy, 2009*). Snow generally covers the basin from November to June. Average seasonal precipitation is about 900 mm, increasing to over 1140 mm at the treeline (*Storr, 1967*), where about 60%-75% falls as snow (*DeBeer and Pomeroy, 2009*). The melt period is generally April to July (*DeBeer and Pomeroy, 2009*). The work by *DeBeer and Pomeroy (2009)* showed that the snow-covered areas (SCA) of the alpine sites such as the Mt. Allan cirque, a north-facing slope, and a south-facing slope were 0.3, 0.4, and 0.1 respectively by mid-June, following a typical winter in 2007.

Measurements conducted over the study period were taken at hydro-meteorological stations in the basin and are summarized in Table 1. Shortwave pyranometers used in this study are shown in Figure 1 and include Apogee SP-110s (spectral response: 280 nm – 2800 nm, cosine correction of  $\pm 1\%$ –5%, absolute accuracy of  $\pm 5\%$ ) at Fisera Ridge, South Meadow, and Hay Meadow; and Delta-T SPN1s (spectral response: 400nm – 2700 nm, cosine correction of  $\pm 2\%$ , resolution 0.6 W m<sup>-2</sup>) at Fisera Ridge and Hay Meadow. All instruments were sampled at a frequency of 0.1 Hz, and the data were averaged and stored every 15 minutes by Campbell Scientific Canada CR3000 dataloggers and Delta-T dataloggers. A time-lapse camera was installed at Fisera Ridge north-facing Mount Collembola and the South Meadow site. The camera was a Pentax K110D digital single lens reflex (DSLR) with a Pentax DA 21 mm F32AL Limited lens that minimizes

radial image distortion. The camera was triggered by a Campbell Scientific Canada CR200 datalogger. Images were taken hourly from 08:00 – 17:00 daily.

A Light Detection And Ranging (LiDAR) elevation dataset at one-metre spatial resolution and 0.15 cm vertical accuracy was available from previous research and is summarized in (*Hopkinson et al.*, 2011). A triangular unstructured mesh with a one-metre tolerance (see next section) was constructed from these LiDAR data.

Because it is not the purpose of this study to test methods for estimating atmospheric transmittance or diffuse radiation, measured direct-beam and diffuse-beam radiation (from the Delta-T SPN1) were used as data for the model. There were no winter-accessible sites with an unobstructed view of the sky that measured both direct irradiance and diffuse irradiance. As a result, no one hydro-meteorological station provided a complete record of incoming solar radiation with no shading. For example, the Hay Meadow site is in shadow early in the morning, whereas the Fisera site is not, with this situation reversing late in the day. In order to provide a complete record of incoming radiation (diffuse and direct) with no shading, measurements from the SPN1 instrument at the Hay Meadow and Fisera sites were spliced together to create a synthetic dataset using Fisera Ridge values from sunrise to noon and Hay Meadow values until sunset. This synthetic dataset represents the irradiance throughout the day that is as free from topographic shadow contamination as possible. The measured direct-beam irradiance data ( $K_{meas}$  [ $\text{W m}^{-2}$ ]) were corrected from flat-plane values to account for measured flat-plane solar zenith angle ( $Z$ ) (*Garnier and Ohmura*, 1968; *Oke*, 1987) such that

$$S \tau = \frac{K_{meas}}{\cos(Z)} \quad (1)$$

where  $S$  ( $\text{W m}^{-2}$ ) is the solar constant,  $Z$  the solar zenith angle, and  $\tau$  is the transmittance of the atmosphere to direct beam solar radiation.

Diffuse radiation was assumed to be isotropic and corrected for the skyview at each triangle by computing the skyview factor, which is the ratio of the diffuse sky irradiance with obstructing terrain to that of an unobstructed sky, for the LiDAR DEM using the algorithm of *Dozier and Frew* (1990) as implemented in the SAGA-GIS software (*SAGA Development Team*, 2007). The values for each triangle vertex were then extracted from this structured mesh, and the average of each triangle’s vertices was used as the skyview for a triangle. Although it is necessary to compute a skyview factor when considering diffuse radiation, this relatively simple hybrid scheme avoids the problems of storing the horizon in every direction for every point and searching through the horizon for every point for every timestep when computing direct-beam shading. Rather, because the skyview is a fixed constant and diffuse shortwave radiation is considered isotropic (no dependence upon solar position), there is no need for directional searches. Therefore the skyview factor can be computed once and used for the entire diffuse irradiance calculation, and the projection technique can be used for the shading location. Reflected irradiance can be important (*Marks and*

*Dozier*, 1992), especially on cloudy days; however it was not considered in this study and solar irradiance was estimated as the sum of diffuse- and direct-beam irradiance.

A snowcovered period was simulated from October 17, 2010 to June 14, 2011 at a 15-minute temporal scale, and a snowmelt period was simulated from April 1, 2011 to June 14, 2011 at a 15-minute temporal scale. Finally, a clear sky day was modeled for February 1, 2011 at 15-minute intervals from sunrise to sunset. This was done to check the performance of the model for a day that did not have any shadows other than those caused by topographic features. For these periods, measured solar irradiance was used at 15-minute intervals and the difference between the self-shading values and the horizon-shadow values was computed. Cumulative energy to the plane of the triangle ( $\text{MJ m}^{-2}$ ) was computed assuming a constant irradiance (temporally and spatially) over the modelling time-step of 15 minutes. An area slightly larger than the MCRB was simulated in order to capture horizon-shadows created from topography outside the basin.

### 3 Model Development

For use in a hydrological model, the spatial domain of interest must be discretized such that a spatial unit, however defined, is connected to other spatial units. A raster dataset (structured mesh), such as that derived from a LiDAR source, may be triangulated such that for the specified domain triangles of variable size represent the topography. Triangle vertices thus have  $x, y, z$  components that represent the elevation of a point in some coordinate system, e.g., UTM. A common and powerful triangulation is Delaunay triangulation; see *Shewchuk* (2002) for a full treatment. Using Delaunay triangulation, the triangulation can be constrained to important characteristics of the model domain such as streams, rivers, and basin deliniation thus guaranteeing their representation. Once complete, a triangulation is essentially a linear interpolant. Thus when creating a triangulation from a structured mesh a tolerance must be specified. This is the maximum difference between the triangle and grid points represented by the triangle. Therefore, stringent tolerances produce a greater number of triangles, and vice versa. Because of this, if the input dataset is of a spatial resolution such that a loss of accuracy is unacceptable, more stringent tolerances must be chosen. Because computational time increases as a function of number of triangles, choosing a tolerance that is too stringent negates some of the performance increases of an unstructured mesh. This results in a balance of acceptable error in the unstructured mesh and computational efficiency. Ideally, the input data would be the LiDAR point cloud, before any further processing was done.

Once the triangulation is constructed, shading locations can be mapped using various methods. In this study, the rotation proposed by *Montero et al.* (2009) is used to determine horizon-shadow locations via Euler rotations; see *Fowles and Cassiday* (2005) for a treatment of Euler angles. The algorithm of

*Montero et al.* (2009) is an extension of the parallel point-plane method originally introduced by *Clarke* (2001). The parallel point-plane algorithm determines horizon-shaded areas as follows. A receiver area is an arbitrarily oriented plane defined in 3-space that can potentially be shadowed, and an obstructer area is an arbitrarily oriented plane in 3-space that can cast a shadow. In this case, the topography is represented by triangles; therefore each triangle is potentially an obstructer and a receiver simultaneously. That is, all parts of the terrain can shade other terrain while being shaded. For this algorithm, the standard  $x, y, z$  Cartesian coordinate system is rotated so that the new vertical coordinate points at the sun. In this rotated configuration, some triangles may be located between the sun and other triangles, and by projecting the rotated coordinate system onto a plane and checking for intersecting triangles, shadow locations can be calculated. Details of this follows.

### 3.1 Mathematical background

Let  $\theta_s$  be the solar elevation and  $\phi_s$  be the solar azimuth (clockwise from north, in radians) at a time  $t$ . Let  $x, y, z$  be a reference coordinate system with  $x$  positive to the east,  $y$  positive to the north, and  $z$  positive in the vertical direction (corresponding to elevation). This initial configuration is shown in Figure 2. Let  $x', y', z'$  be a coordinate system obtained by performing an XZX series of Euler rotations on the coordinate system  $x, y, z$  to align the  $z'$  axis with the solar vector.

For a given angle  $\psi$ , let  $\mathbf{R}_x(\psi)$  be the  $x$  rotation matrix and  $\mathbf{R}_z(\psi)$  be the  $z$  rotation matrix given as

$$\mathbf{R}_x(\psi) = \begin{bmatrix} 1 & 0 & 0 \\ 0 & \cos \psi & -\sin \psi \\ 0 & \sin \psi & \cos \psi \end{bmatrix}, \quad (2)$$

and

$$\mathbf{R}_z(\psi) = \begin{bmatrix} \cos \psi & -\sin \psi & 0 \\ \sin \psi & \cos \psi & 0 \\ 0 & 0 & 1 \end{bmatrix}. \quad (3)$$

Then the rotation from  $x, y, z$  to  $x', y', z'$  is done via the Euler rotations

$$\mathbf{R} = \mathbf{R}_x\left(-\frac{\pi}{2} + \theta_s\right) \mathbf{R}_z(-\pi + \phi_s) \mathbf{R}_x(0), \quad (4)$$

$$\mathbf{R} = \begin{bmatrix} \cos(-\pi + \phi_s) & \sin(-\pi + \phi_s) & 0 \\ -\cos\left(-\frac{\pi}{2} + \theta_s\right) \sin(-\pi + \phi_s) & \cos\left(-\frac{\pi}{2} + \theta_s\right) \cos(-\pi + \theta_s) & \sin\left(-\frac{\pi}{2} + \theta_s\right) \\ \sin\left(-\frac{\pi}{2} + \theta_s\right) \sin(-\pi + \phi_s) & -\sin\left(-\frac{\pi}{2} + \theta_s\right) \cos(-\pi + \theta_s) & \cos\left(-\frac{\pi}{2} + \theta_s\right) \end{bmatrix}. \quad (5)$$

The rotation  $\mathbf{R}$  is applied to each triangle's vertex. The result of this rotation is a transformed  $x', y', z'$  coordinate system that defines triangles, with

respect to the solar vector, further from the sun as having smaller  $z'$  values and triangles closer to the sun as having a larger  $z'$  values. These rotated triangles are projected onto the  $x'y'$  plane and are interpreted as triangles in two dimensions for the purpose of the triangle-triangle intersection test. For the purpose of visualization, the triangles were coloured according to an average of their three vertex  $z'$  values that was then normalized to values between 0 and 1. An example of this is shown in Figure 3. The scene is shown with the observer between the sun and the terrain and along the solar vector. Triangles with high values (red) are the closest to the sun, and triangles with low values (blue) are furthest away from the sun. The scene is shown from a different perspective in Figure 4, with the observer located looking directly into the basin (approximately west), with the sun on the left of the scene. The ordering of the triangles obtained from the  $z'$  values allows for obscuring triangles to be detected. For computational efficiency when determining whether two triangles intersect, only triangles with similar  $x', y'$  values need to be compared. Because the original algorithm in *Montero et al. (2009)* used a different mesh type than the Delaunay mesh used herein, the algorithm was modified accordingly. The rotated triangles are fit with a minimum bounding rectangle that is segmented into  $m$  rows and  $n$  columns creating  $mn$  regions. Triangles are assigned to a region, and if a triangle falls into more than one region, it is considered in each region it intersects. To determine intersection between triangles, the vertices and circumcentre of each triangle are used as detection points. The triangles of each region are checked in order of largest  $z'$  to smallest  $z'$  against the remaining triangles in the region. If a triangle lies in front of another triangle (based on their respective  $z'$  values) the one with the larger  $z'$  value is checked for an intersection with the triangle behind it. If intersection is detected, the triangle with the smaller  $z'$  value is marked as shaded with a binary shadow mask, i.e., shaded=0 and non-shaded=1. If a triangle is already marked as shadowed, it is not checked further to see if it is multiply shadowed, but it is still used to determine other shadows.

Each triangle's irradiance was calculated using the standard cosine-correction (*Garnier and Ohmura, 1968; Oke, 1987*). To calculate the direct-beam irradiance to a triangle (considered uniform over the triangle) the following equations were used. Let  $\hat{\mathbf{n}}$  be the unit normal vector to a triangle's surface. Then the angle  $\Theta_{sn}$  between the surface normal and the unit solar vector  $\hat{\mathbf{s}}$  is given by

$$\Theta_{sn} = \arccos(\hat{\mathbf{n}} \cdot \hat{\mathbf{s}}) \quad (6)$$

where  $\hat{\mathbf{s}}$ , in a Cartesian coordinate system, is given by:

$$\hat{\mathbf{s}} = \begin{bmatrix} \cos \theta_s \sin \phi_s \\ \cos \theta_s \cos \phi_s \\ \sin \theta_s \end{bmatrix}. \quad (7)$$

The self-shaded direct-beam irradiance ( $K_s$  [W m<sup>-2</sup>]) is then computed as

$$K_s = S \tau \cos(\Theta_{sn}) \quad (8)$$

where  $S$   $\tau$ , as per Equation 1, are the corrected measured data. Considering the binary shadow mask,  $\zeta$ , horizon-shaded direct-beam irradiance ( $K_h$  [ $\text{W m}^{-2}$ ]) was then computed as

$$K_h = \zeta K_s. \quad (9)$$

To account for self-shading, if  $\cos(\Theta_{sn})$  was less than zero, i.e., the triangle was facing  $90^\circ$  or more away from the sun, the triangle was marked as self-shaded and assigned a direct-beam irradiance of  $0 \text{ W m}^{-2}$ .

### 3.2 Computational complexity

The computational complexity of the horizon-shading algorithm was determined analytically to be  $\mathcal{O}(N \log N)$ , where  $N$  is the number of triangles in the unstructured mesh. An empirical verification of this complexity was performed by running the model for one time step (February 1, 2011 at 16:30) for a range of meshes ranging from 851 triangles to 544507 triangles. The results are shown in Figure 5, where the black symbols are the measured wall-clock times and the grey dashed line is a curve of best fit of the form  $t = a_0 + a_1 N + a_2 (N \log N)$ . The form of the fit is based on an analytical complexity analysis of the algorithm and has an adjusted  $R^2$  of 0.99994. Although the algorithm is parallelizable, and this fact is exploited when running the algorithm in practice, the complexity analysis and timing information reported are for a serial implementation. The benchmark tests were performed on an Intel Xeon W3520 processor with a clock speed of 2.66 GHz and 16 GB of DDR3 RAM running Ubuntu 10.04 LTS. The Intel C++ compiler version 12.0.4 20110427 was used with level-3 optimization with SSE 4.2 instruction-set compatibility enabled. Timings were taken using the `clock_gettime` function. The values reported are the minimum times of fifty runs.

## 4 Shadow location and movement

Figure 6 shows timelapse images of the movement of a horizon-shadow across the South Meadow site on February 1, 2011 from 16:00 to 17:00. The South Meadow site is the clearing indicated by the red arrow. The image is taken from Fisera Ridge North viewing down the valley, roughly in an easterly direction; see Figure 1. The large shadow visible in both images is cast from Fisera Ridge. South Meadow is a south-facing slope and as a result generally receives relatively high irradiance. A sharp decrease in irradiance at South Meadow is observed once the Fisera Ridge shadow crosses the site. A binary shadow map was created for the clear-sky day February 1, 2011 at 16:30 and is shown in Figure 7. Areas in black, grey, and white are the horizon-, self-, and non-shadowed areas respectively, with elevation contours every 100 m of elevation. The South Meadow site is indicated. This shows the modelled horizon-shadow crossing the South Meadow site as shown in Figure 6. There are misclassifications of some triangles, visible as the lone shaded triangles. This is the result of imprecisions

in the triangle detection scheme. Future work will help refine this algorithm and should significantly cut down on these occasional misclassifications by using more robust criteria for detecting shadows.

In order to determine whether the model can accurately predict the timing of the shadow shown in Figure 6, point-scale irradiance from the same model day is shown in Figure 8. This figure shows the irradiance measured at the South Meadow station (fine dotted line), the modelled irradiance using the horizon-shadow algorithm (dashed line), and the modelled irradiance using only the self-shading algorithm (solid line). The model result from the horizon-shadows algorithm has a sharp decrease in irradiance at approximately 16:30 when the horizon-shadow from Fisera Ridge crosses South Meadow. This decrease in irradiance corresponds well to that shown in the time-lapse photos in Figure 6. The peak value differences are attributed to the fact that the triangle upon which the South Meadow site lies in the model is not perfectly flat like the measuring pyrometer resulting in slightly higher direct-beam irradiance. As well, because different instruments were used for South Meadow and the synthetic input data set, different amounts of reflected irradiance are present as well as differences in the actual instruments.

Snow in this area is not affected by wind-borne dust and hence albedos remain higher than many published values, even during melt periods (*Helgason and Pomeroy, 2012*). Many published low albedo values for snow during melt are contaminated by snow-free area and the snow covered area (SCA) albedo is known to decay at a much slower rate than the areal albedo (*O'Neill and Gray, 1973; Male and Granger, 1981; Pomeroy et al., 1998*). *Pomeroy et al. (1998)* show that when SCA corrections are employed then albedo during melt can remain at 0.85. It should be noted that a fixed albedo will eventually be wrong, as late melt will have a significantly lower albedo than pre-melt due to albedo decay. For this analysis however, an albedo of 0.8 (*Oke, 1987*) is assumed.

#### 4.1 Point-scale difference

The point-scale difference in irradiance between the models was averaged on a monthly basis over the course of the seasonal period (October–June). The largest average difference was  $4.8 \text{ W m}^{-2}$  during the period of December to February, occurring during periods with the lowest solar angles when the largest shadows are cast by the surrounding topography. Differences decreased over the winter and spring through to the summer, with a monthly average difference of less than  $1 \text{ W m}^{-2}$  in June. This difference was accumulated over the season and is shown in Figure 9 as the dashed line. The difference accumulated in a linear fashion throughout the winter due to the long horizon-shadows from the low solar angles. With the arrival of spring and larger solar angles, differences became smaller and the cumulative difference curve leveled off. Shown in Figure 9 is the cumulative difference between the self-shading and horizon-shading algorithms for the October–June season (dashed line) and the April–June spring period (solid line). Over the season of October–June, irradiance at the South Meadow site was over-estimated by a total of  $52 \text{ MJ m}^{-2}$  by the self-shading

model. Some of this irradiance would be absorbed by the snowpack and would contribute to an overestimation of the internal energy of the snowpack (i.e., the snowpack would be too warm) over the winter and hence a ripening and melting of snow that are too early in the spring. Even when melt simulations are started in spring from correct initial conditions, there would be a small, but potentially important, difference in estimations of snowmelt by ignoring horizon-shading. It is observed that a large portion of the cumulative difference develops in early to mid-April, with diminishing additional differences through late May into early June. During this spring period, the cumulative difference in irradiance due to shading during this melt period is  $4.5 \text{ MJ m}^{-2}$ ; this could translate into a snowmelt difference of  $2.69 \text{ kg m}^{-2}$  if all of the net solar difference were applied to phase change. These differences introduced when horizon shading is not accounted for results in a cumulative difference between models over the season and the melt period. The difference in irradiance is predominantly of the same sign and generally does not average or cancel out over the season.

## 4.2 Basin-wide difference

Cumulative differences between self- and horizon-shading algorithms for the melt period from April 1, 2011 to June 14, 2011 were considered for the entire simulation domain (206580 triangles). For this period, 99% of the differences are less than  $500 \text{ kg m}^{-2}$  with a peak difference of  $1600 \text{ kg m}^{-2}$  predicted over a small fraction of the basin. This peak is equivalent in magnitude to more than the maximum snowfall in the highest elevations of the basin. Using the same assumptions as above (albedo, et cetera), the mean phase change mass over the basin was  $14.4 \text{ kg m}^{-2}$ .

In Figure 10, the seasonal (October–June) cumulative difference between modelled irradiance using the two shading algorithms is shown in terms of net solar radiation for snowmelt, assuming continuous snowcover and an albedo of 0.8, and as the mass of melted snow, assuming that all net solar radiation is applied to snowmelt. For the majority of this period, low solar angles cast large shadows onto the south-facing slopes, providing the bulk of the difference. The south-facing slope of Mt. Collembola, the slope on which South Meadow lies, is a frequent recipient of horizon-shadows from Fisera Ridge. The south-facing slopes of the Mt. Allan cirque, shaded from the surrounding ridge line, are also areas where the irradiance is over-predicted by the self-shading algorithm. The right side of the large ‘V’ notch on Mt. Collembola is strongly over-predicted, and time-lapse camera observations showed that this large shadow was associated with an abrupt transition between snow and snow-free areas in the notch. In the top left (NW) corner is an area outside of the MCRB. It is a ‘U’ shaped valley that is almost always in the shadow cast from the back of Mt. Collembola. This resulted in a large over-prediction of irradiance throughout the melt period if horizon-shadows are not considered — in fact, most of the large errors are found in this valley. The south face of the southern ridge line (at about  $7.27 \times 10^6 \text{ m E}$ ) is shown to have some of the largest differences due to horizon-shadows from the ridge line. When considering the mean difference (in  $\text{MJ m}^{-2}$ ) of each

triangle with respect to triangle azimuth (clockwise from North), the largest differences are observed to be on east- and south-facing slopes.

For the melt period of April–June 2011, Figure 11 shows the difference between self-shading and horizon-shading models, expressed in terms of net solar radiation for snowmelt, assuming continuous snowcover and an albedo of 0.8, assuming that all net solar radiation is applied to snowmelt. South-facing slopes are again predicted to be areas of large differences. The south-facing slope of South Meadow is shown to have a large difference, and in general the basin exhibits a similar pattern to that of the seasonal model run. However, a notable change is that the north-facing southern ridge (at about  $7.27 \times 10^6$  m E) has a large cumulative difference. Generally this area should be self-shaded; however, due to the higher solar angles the triangle faces are not fully facing away from the sun. Although this results in triangles with low values of  $\cos(\Theta_{sn})$ , these values are not so low as to generate self-shadows. Thus during the morning as the sun passes through to the south, the direct-beam irradiances calculated using self-shading are not  $0 \text{ W m}^{-2}$ , and thus there is a large over-prediction of irradiance. Because of these accumulated differences, higher-than-estimated snowmelt would likely be observed in this valley if only self-shading algorithms were used, and the persistence of late winter snowpacks would not be appropriately modelled.

### 4.3 Comparison with measured values

*DeBeer and Pomeroy* (2009) presented the results from a set of snow surveys conducted in the Mt. Allan cirque over the later winter and spring of 2007. The cirque is on the eastern side of Mt. Allan and is approximately  $0.6 \text{ km}^2$  in area. Extensive snow surveys were made on March 29–30, 2007, just before the main snowmelt period. These values are taken to be the pre-melt SWE values and are summarized in Table 2. The irradiance model for April–June 2011 was applied to the cirque and the cumulative difference between the self-shading and horizon-shading algorithms was computed. The difference is expressed as the snow mass that would undergo phase change if all energy were applied to melt (mm SWE) with the above stated assumptions. For the slopes of azimuth  $0^\circ$ – $40^\circ$ , the average difference was 19.7 mm, and for the slopes of azimuth  $140^\circ$ – $180^\circ$ , the average difference was 16.33 mm. For the north- and south-facing slopes, the difference equates to 6.0% and 11.4% of total pre-melt SWE respectively. The cumulative difference is 66.4% of the total pre-melt SWE for the shallow south-facing slope.

*DeBeer and Pomeroy* (2009) identified in the cirque that the spatial variability of the surface energetics due to slope and aspect had a strong effect on snowmelt rates and snow cover depletion (SCD). Because of the patchiness of SCD, correct prediction of the surface energy balance is required, and *DeBeer and Pomeroy* (2009) suggest that melt energetics on slope units should be considered further. Although timing issues in SCD were generally attributed to errors in the log-normal fit, it was suggested that improvements might also arise from more accurate melt simulations in sheltered areas. Slope units were con-

sidered in *DeBeer and Pomeroy* (2010) where it was shown that consideration of a slope based melt energetics substantially improved the SCD calculations. Because there is some dependence on the magnitude of the difference between irradiance models and slope, it is possible that SCD calculations would improve further when coupled with horizon-shaded irradiance models.

## 5 Conclusion

An unstructured mesh was used to discretize a Canadian Rockies complex terrain site, the Marmot Creek Research Basin, using a  $1\text{m}^2$  LiDAR-derived DEM as input. In order to capture the horizon-shadows of surrounding topographic features, the parallel-point plane method used by *Clarke* (2001) and expanded upon by *Montero et al.* (2009) was implemented to model irradiance in complex terrain. A new coordinate system, aligned with the solar position, was created through the use of a rotated coordinate system using Euler angles. The effects of surrounding mountain topography on irradiance in Marmot Creek were substantial. Overall, there was a systematic over-prediction of irradiance when not considering horizon-shadows. Horizon-shadow and self-shading irradiance predictions were compared at a point scale to measured irradiance observations and time-lapse photography at the South Meadow site in Marmot Creek Research Basin on the clear-sky day February 1, 2011. It was found that the shadow passage over the South Meadow site at 16:30 was correctly modelled by the horizon-shadow algorithm.

At this point scale for this day, neglecting horizon-shadows and only modelling with self-shadows resulted in a peak difference of  $258\text{ W m}^{-2}$  and a mean difference of  $26.2\text{ W m}^{-2}$  in irradiance, averaged between sunrise and sunset. Modelled over the season from October to June, this resulted in a total cumulative difference in energy of  $52\text{ MJ m}^{-2}$  and, in the snowmelt period of April to June,  $4.5\text{ MJ m}^{-2}$ . This corresponded to a potential of  $2.69\text{ kg m}^{-2}$  if all of the net solar difference were applied to phase change as snowmelt, assuming a continuous snowcover, an albedo of 0.8. At the basin scale for the snowmelt period of April-June, the mean triangle potential snowmelt mass difference was  $14.4\text{ kg m}^{-2}$  assuming the same as above. Compared to pre-melt SWE values from 2007 following *DeBeer and Pomeroy* (2009) for the Mt. Allan cirque, this mean cumulative difference is 6.0% and 11.4% for north- and south-facing slopes respectively of total pre-melt SWE. The cumulative difference is 66.4% of the total pre-melt SWE for the shallow south-facing slope.

## References

Braun, J., and M. Sambridge (1997), Modelling landscape evolution on geological time scales: a new method based on irregular spatial discretization, *Basin Research*, 9(1), 27–52.

- Carey, S., and M.-k. Woo (1998), Snowmelt hydrology of two subarctic slopes, southern Yukon, Canada, *Nordic Hydrology*, 29(4), 331.
- Chueca, J., and A. Julián (2004), Relationship between solar radiation and the development and morphology of small cirque glaciers (Maladeta Mountain massif, Central Pyrenees, Spain), *Geografiska Annaler: Series A, Physical Geography*, 86(1), 81–89.
- Clarke, J. A. (2001), *Energy Simulation in Building Design*, 2nd ed., 362 pp., Butterworth-Heinemann, Oxford, UK.
- Coquillart, S., and M. Gangnet (1984), Shaded display of digital maps, *IEEE Computer Graphics and Applications*, 4, 35–42.
- Davies, T. D., P. Brimblecombe, M. Tranter, S. Tsiouris, C. E. Vincent, P. Abrahams, and I. L. Blackwood (1987), The removal of soluble ions from melting snowpacks, in *Seasonal Snowcovers: Physics, Chemistry, Hydrology*, edited by H. G. Jones and W. J. Orville-Thomas, pp. 337–392, D. Reidel Publishing Company, Dordrecht, Holland.
- Davison, B., S. Pohl, P. Dornes, P. Marsh, A. Pietroniro, and M. MacKay (2006), Characterizing snowmelt variability in a land-surface-hydrologic model, *Atmosphere-Ocean*, 44(3), 271–287.
- DeBeer, C. M., and J. W. Pomeroy (2009), Modelling snow melt and snowcover depletion in a small alpine cirque , Canadian Rocky Mountains, *Hydrological Processes*, 23(18), 2584– 2599.
- DeBeer, C. M., and J. W. Pomeroy (2010), Simulation of the snowmelt runoff contributing area in a small alpine basin, *Hydrology and Earth System Sciences*, 14(7), 1205–1219.
- Dornes, P. F., J. W. Pomeroy, A. Pietroniro, S. K. Carey, and W. L. Quinton (2008), Influence of landscape aggregation in modelling snow-cover ablation and snowmelt runoff in a sub-arctic mountainous environment, *Hydrological Sciences Journal*, 53(4), 725–740.
- Dozier, J., and J. Frew (1990), Rapid calculation of terrain parameters for radiation modeling from digital elevation data, *IEEE Transactions on Geoscience and Remote*, 28(5).
- Dozier, J., J. Bruno, and P. Downey (1981), Faster Solution to the Horizon Problem, *Computers and Geosciences*, 7(2), 145–151.
- Dymond, C. (2002), Mapping vegetation spatial patterns from modeled water, temperature and solar radiation gradients, *ISPRS Journal of Photogrammetry and Remote Sensing*, 57(1-2), 69–85, doi:10.1016/S0924-2716(02)00110-7.
- Essery, R., and D. Marks (2007), Scaling and parametrization of clear-sky solar radiation over complex topography, *Journal of Geophysical Research*, 112(D10), 1–12, doi:10.1029/2006JD007650.

- Fowles, G. R., and G. L. Cassiday (2005), *Analytical Mechanics*, 7th ed., 544 pp., Thomson Brooks/Cole, Belmont, USA.
- Frew, J. E. (1990), The Image Processing Workbench, Doctor of philosophy, University of California.
- Fu, P., and P. M. Rich (1999), Design and implementation of the Solar Analyst: an ArcView extension for modeling solar radiation at landscape scales, in *Proceedings of the 19th Annual ESRI User Conference*, pp. 1–33, San Diego, USA.
- Garnier, B. J., and A. Ohmura (1968), A Method of Calculating the Direct Shortwave Radiation Income of Slopes, *Journal of Applied Meteorology*, 7(5), 796–800, doi:10.1175/1520-0450(1968)007;0796:AMOCTD;2.0.CO;2.
- Golding, D. L. (1970), Research results from Marmot Creek experimental watershed, Alberta, Canada, in *Symposium on the results of research on representative and experimental basins*, pp. 397–404, IASH-UNESCO, Wellington, New Zealand.
- Gray, D. M., and D. H. Male (1981), *Handbook of Snow: Principles, Processes, Management, and Use*, 776 pp., Pergamon Press, Toronto, Canada.
- Gray, D. M., B. Toth, L. Zhao, J. W. Pomeroy, and R. J. Granger (2001), Estimating areal snowmelt infiltration into frozen soils, *Hydrological Processes*, 15(16), 3095–3111.
- Groisman, P., and T. Davies (2001), Snow cover and the climate system, in *Snow Ecology: an Interdisciplinary Examination of Snow-covered Ecosystems*, edited by H. Jones, J. Pomeroy, D. Walker, and R. Hoham, chap. 1, pp. 1–44, Cambridge University Press, Cambridge, UK.
- Helgason, W., and J. W. Pomeroy (2012), Characteristics of the near surface boundary layer within a mountain valley during winter, *Journal of Applied Meteorology and Climatology*, 51(3), 583–597, doi: <http://dx.doi.org/10.1175/JAMC-D-11-058.1>.
- Hetrick, W., P. Rich, and S. Weiss. (1993), Modeling insolation on complex surfaces, in *Thirteenth Annual ESRI User Conference*, vol. 2, pp. 447–458.
- Hopkinson, C., J. Pomeroy, C. DeBeer, C. Ellis, and A. Anderson (2011), Relationships between snowpack depth and primary LiDAR point cloud derivatives in a mountainous environment, in *Remote Sensing and Hydrology 2010*, IAHS Publ. 3XX, Jackson Hole, Wyoming, USA.
- Ivanov, V., E. Vivoni, R. Bras, and D. Entekhabi (2004), Preserving high-resolution surface and rainfall data in operational-scale basin hydrology: a fully-distributed physically-based approach, *Journal of Hydrology*, 298(1-4), 80–111, doi:10.1016/j.jhydrol.2004.03.041.

- Kumar, M., G. Bhatt, and C. Duffy (2009), An efficient domain decomposition framework for accurate representation of geodata in distributed hydrologic models, *International Journal of Geographical Information Science*, *23*(12), 1569–1596.
- MacDonald, M. K., J. W. Pomeroy, and A. Pietroniro (2010), On the importance of sublimation to an alpine snow mass balance in the Canadian Rocky Mountains, *Hydrology and Earth System Sciences*, *14*(7), 1401–1415.
- Male, D. H., and R. J. Granger (1981), Snow surface-energy exchange, *Water Resources Research*, *17*(3), 609–627.
- Marks, D., and J. Dozier (1992), Climate and energy exchange at the snow surface in the alpine region of the Sierra Nevada, 2, Snow cover energy balance, *Water Resources Research*, *28*(11), 3043–3054.
- Marshak, A., and A. B. Davis (2005), *3D Radiative Transfer in Cloudy Atmospheres*, 686 pp., Springer-Verlag, Berlin, Germany.
- Montero, G., J. Escobar, E. Rodriguez, R. Montenegro, and E. Rodríguez (2009), Solar radiation and shadow modelling with adaptive triangular meshes, *Solar Energy*, *83*(7), 998–1012, doi:10.1016/j.solener.2009.01.004.
- Munro, D. S., and G. J. Young (1982), An operational net shortwave radiation model for glacier basins, *Water Resources Research*, *18*(2), 220–230, doi:10.1029/WR018i002p00220.
- O’Callaghan, J. F., and D. Marks (1984), The extraction of drainage networks from digital elevation data, *Computer Vision, Graphics, and Image Processing*, *28*(3), 323–344.
- Oke, T. (1987), *Boundary layer climates*, second ed., 435 pp., University Press, Cambridge, UK.
- Oliphant, A. J., R. A. Spronken-Smith, A. P. Sturman, and I. F. Owens (2003), Spatial Variability of Surface Radiation Fluxes in Mountainous Terrain, *Journal of Applied Meteorology*, *42*(1), 113–128.
- O’Neill, A., and D. Gray (1973), Solar radiation penetration through snow, in *UNESCO-WMO-IAHS Symposia on the Role of Snow and Ice in Hydrology*, pp. 227–249, IAHS Press, Wallingford, UK.
- Petty, G. W. (2006), *A First Course in Atmospheric Radiation*, 2nd ed., 472 pp., Sundog Publishing, Madison, USA.
- Pohl, S., P. Marsh, and A. Pietroniro (2006), Spatial temporal variability in solar radiation during spring snowmelt, *Nordic Hydrology*, *37*(1), 1–19, doi:10.2166/nh.2005.026.

- Pomeroy, J., D. Gray, K. Shook, B. Toth, R. Essery, A. Pietroniro, and N. Hedstrom (1998), An evaluation of snow accumulation and ablation processes for land surface modelling, *Hydrological Processes*, *12*, 2339–2367.
- Pomeroy, J. W., B. Toth, R. J. Granger, N. R. Hedstrom, and R. L. H. Essery (2003), Variation in Surface Energetics during Snowmelt in a Subarctic Mountain Catchment, *Journal of Hydrometeorology*, *4*(4), 702–719, doi:10.1175/1525-7541(2003)004;0702:VISEDJ;2.0.CO;2.
- Ranzi, R., and R. Rosso (1995), Distributed estimation of incoming direct solar radiation over a drainage basin, *Journal of Hydrology*, *166*(3-4), 461–478, doi:10.1016/0022-1694(94)05099-J.
- Romero, L., S. Tabik, J. Vias, and E. Zapata (2008), Fast clear-sky solar irradiation computation for very large digital elevation models, *Computer Physics Communications*, *178*(11), 800–808, doi:10.1016/j.cpc.2008.01.048.
- Ryerson, C. (1984), Mapping Solar Access in High Relief Areas for Regional Energy Planning, *The Professional Geographer*, *36*(3), 345–352.
- SAGA Development Team (2007), System for Automated Geoscientific Analyses (SAGA GIS).
- Shewchuk, J. (1996), Triangle: Engineering a 2D quality mesh generator and Delaunay triangulator, in *Applied Computational Geometry Towards Geometric Engineering*, edited by G. Goos, J. Hartmanis, and J. van Leeuwen, pp. 203–222, Springer Berlin / Heidelberg, doi:10.1007/BFb0014474.
- Shewchuk, J. (2002), Delaunay refinement algorithms for triangular mesh generation, *Computational Geometry*, *22*(1-3), 21–74, doi:10.1016/S0925-7721(01)00047-5.
- Stewart, I. (2009), Changes in snowpack and snowmelt runoff for key mountain regions, *Hydrological Processes*, *23*(1), 78–94, doi:10.1002/hyp.
- Stewart, J. (1998), Fast horizon computation at all points of a terrain with visibility and shading applications, *IEEE Transactions on Visualization and Computer Graphics*, *4*(1), 82–93, doi:10.1109/2945.675656.
- Storr, D. (1967), Precipitation variations in a small forested watershed, in *Proc 35th Annual Western Snow Conference 18-20 April*, pp. 11–17, Boise, Idaho.
- Tabik, S., L. F. Romero, and E. L. Zapata (2011), High-performance three-horizon composition algorithm for large-scale terrains, *International Journal of Geographical Information Science*, *25*(4), 541–555, doi:10.1080/13658810903149995.
- Tachikawa, Y., M. Shiiba, and T. Takasao (1994), Development of a Basin Geomorphic Information System Using a Tin-Dem Data Structure, *Journal of the American Water Resources Association*, *30*(1), 9–17, doi:10.1111/j.1752-1688.1994.tb03268.x.

- Tucker, G. (2001), An object-oriented framework for distributed hydrologic and geomorphic modeling using triangulated irregular networks, *Computers & Geosciences*, 27(8), 959–973, doi:10.1016/S0098-3004(00)00134-5.
- Varley, M. J., K. J. Beven, and H. R. Oliver (1996), Modelling Solar Radiation in Steeply Sloping Terrain, *International Journal of Climatology*, 16(1), 93–104, doi:10.1002/(SICI)1097-0088(199601)16:1<93::AID-JOC992>3.3.CO;2-K.
- Wallace, J. M., and P. V. Hobbs (2006), *Atmospheric Science: An Introductory Survey*, 2nd ed., Elsevier Inc, Burlington, MA.
- Willson, R. C. (2003), Secular total solar irradiance trend during solar cycles 2123, *Geophysical Research Letters*, 30(5), doi:10.1029/2002GL016038.
- Woo, M., W. R. Rouse, R. E. Stewart, and J. M. R. Stone (2008), The Mackenzie GEWEX Study: A Contribution to Cold Region Atmospheric and Hydrologic Sciences, in *Cold Region Atmospheric and Hydrologic Studies Volume 1: Atmospheric Dynamics*, edited by M.-k. Woo, chap. 1, pp. 1–22, Springer-Verlag, Berlin, Germany.
- Woo, M.-k., and K. Young (2004), Modeling arctic snow distribution and melt at the 1 km grid scale., *Nordic Hydrology*, 35(August 2003), 295–307.

## 6 List of symbols

- $\theta_s$  Solar elevation (radians)
- $\phi_s$  Solar azimuth (radians, clockwise from North)
- $x, y, z$  Standard Cartesian coordinate system
- $x', y', z'$  Rotated Cartesian coordinate system
- $\mathbf{R}_x$   $x$  rotation matrix
- $\mathbf{R}_z$   $z$  rotation matrix
- $\hat{\mathbf{n}}$  Triangle surface unit-normal vector
- $\hat{\mathbf{s}}$  Solar beam unit vector
- $\Theta_{sn}$  Angle between  $\hat{\mathbf{s}}$  and  $\hat{\mathbf{n}}$  (radian)
- $K_s$  Self-shaded direct-beam irradiance ( $\text{W m}^{-2}$ )
- $K_h$  Horizon-shaded direct-beam irradiance ( $\text{W m}^{-2}$ )
- $K_{meas}$  Measured direct-beam irradiance ( $\text{W m}^{-2}$ )
- $\zeta$  Binary horizon-shaded mask
- $S$  Solar constant ( $1368 \text{ W m}^{-2}$ )
- $Z$  Zenith angle (radians)

Table 1: Listing of the hydro-meteorological stations at Marmot Creek Research Basin used in this study, with a list of instruments deployed at each site. The CR dataloggers are manufactured by Campbell Scientific Canada, the GP1 dataloggers by Delta-T.

<b>Name</b>	<b>Elevation(m.a.s.l)</b>	<b>Instrumentation</b>	<b>Datalogger</b>
Fisera Ridge	2318	SP-110, SPN1	CR3000, GP1
Fisera Ridge North	2311	SP-110, camera	CR200X
Hay Meadow	1429	SP-110, SPN1	CR3000, GP1
South Meadow	2235	SP-110	CR200X

Table 2: Listing of the pre-melt snow water equivalent for the Mt. Allan cirque following (*DeBeer and Pomeroy, 2009*)

<b>Survey location</b>	<b>SWE (mm)</b>	<b>Average aspect (°)</b>	<b>Average slope (°)</b>
North-facing slope	329.3	20	30
South-facing slope	142.8	160	23
South-facing (shallow SWE)	24.6	-	-
South-facing (deep SWE)	339.8	-	-
All surveys	427.2	-	-

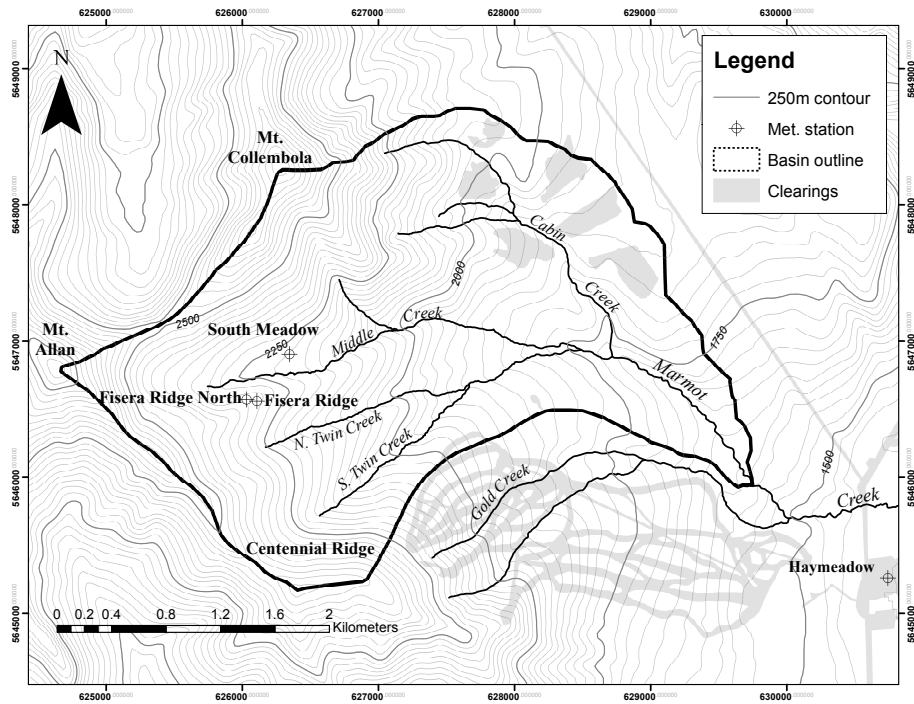


Figure 1: Marmot Creek Research Basin, Kananaskis Valley, Alberta at  $50.96^{\circ}$  N and  $115.21^{\circ}$  W in the Canadian Rocky Mountains. Locations of meteorological stations used in this study are shown along with major topographical features, stream channels, and man-made clearings.

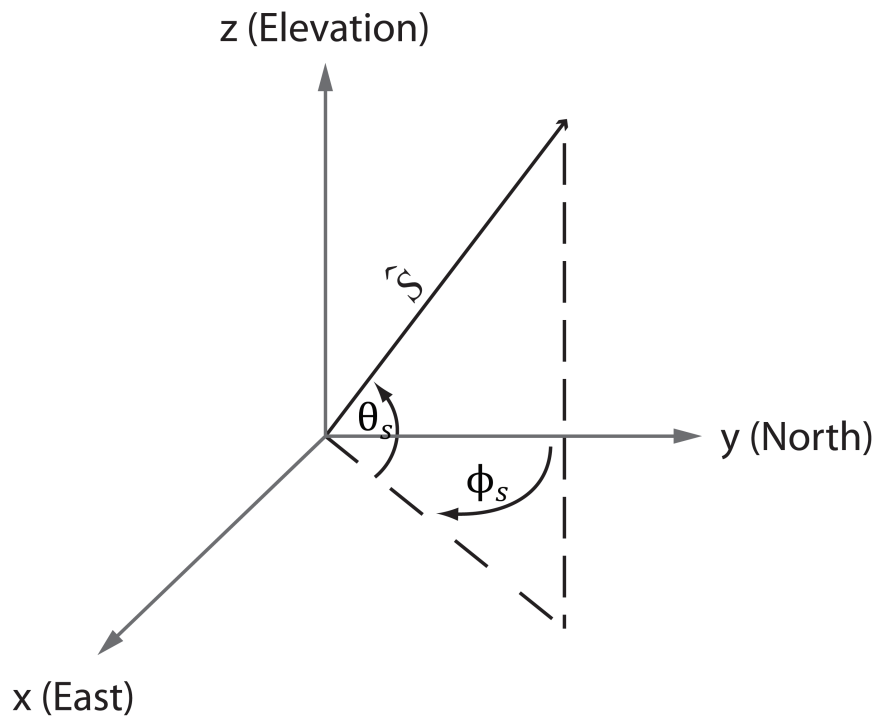


Figure 2: The initial coordinate system configuration of  $x, y, z$ , where  $\theta_s$  is the solar elevation and  $\phi_s$  is the solar azimuth (clockwise from north). The  $x$ -axis is positive to the east, the  $y$ -axis is positive to the north, and the  $z$ -axis is positive in the vertical direction (elevation).

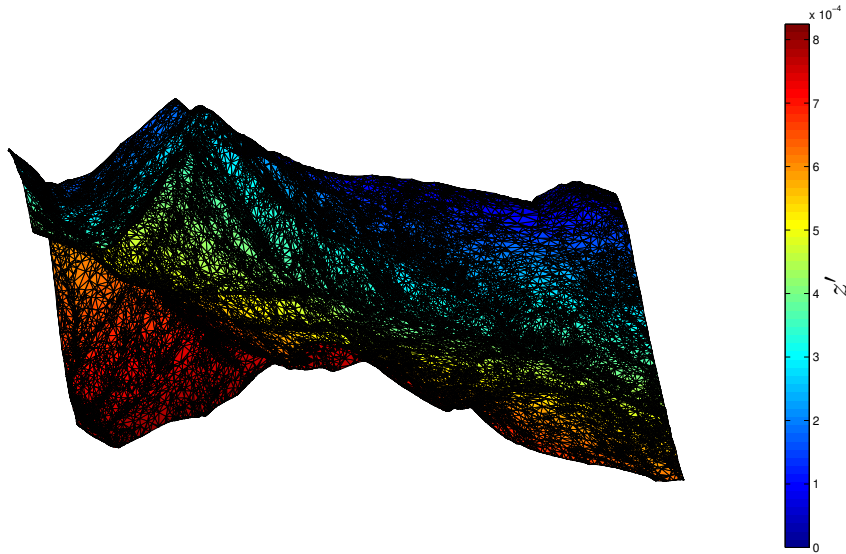


Figure 3: Result of the  $x, y, z$  coordinate system rotated to  $x', y', z'$  where  $z'$  is aligned with the solar vector. The colouring is the average of the  $z'$  values for each of the triangles' vertices, normalized to values between 0 and 1, where triangles with larger  $z'$  values (closer to the sun along the solar vector) are in red and triangles with smaller  $z'$  values (farther from the sun) are in blue. Scene is shown from a perspective aligned with the solar vector. Model time: Feb 1, 2011 at 13:30 (local), looking north-east into the image.

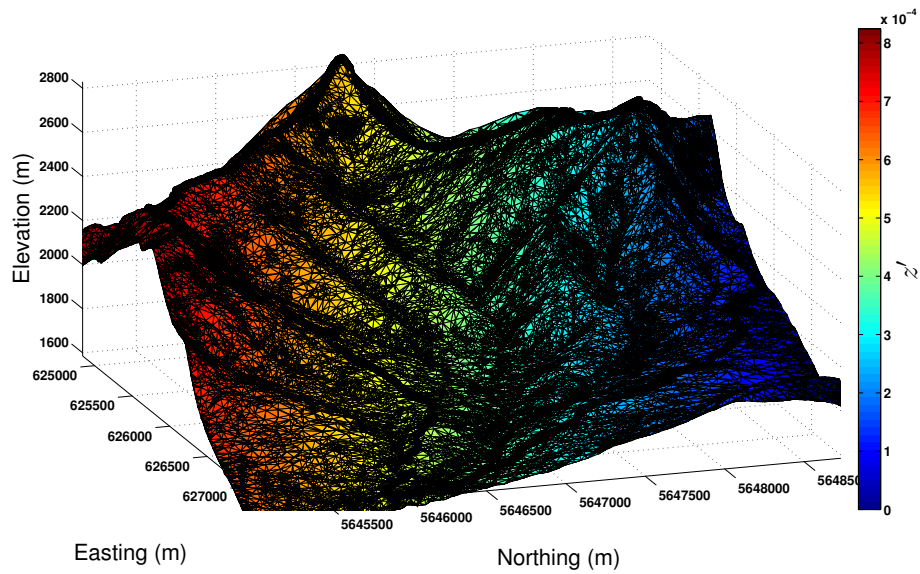


Figure 4: Result of the  $x, y, z$  coordinate system rotated to  $x', y', z'$  where  $z'$  is aligned with the solar vector. The colouring is the average of the  $z'$  values for each of the triangles' vertices, normalized to values between 0 and 1, where triangles with larger  $z'$  values (closer to the sun along the solar vector) are in red and triangles with smaller  $z'$  values (farther from the sun) are in blue. Scene is shown from the perspective of looking approximately west towards the Marmot Creek Basin in the black outline. Model time: Feb 1, 2011 at 13:30 (local).

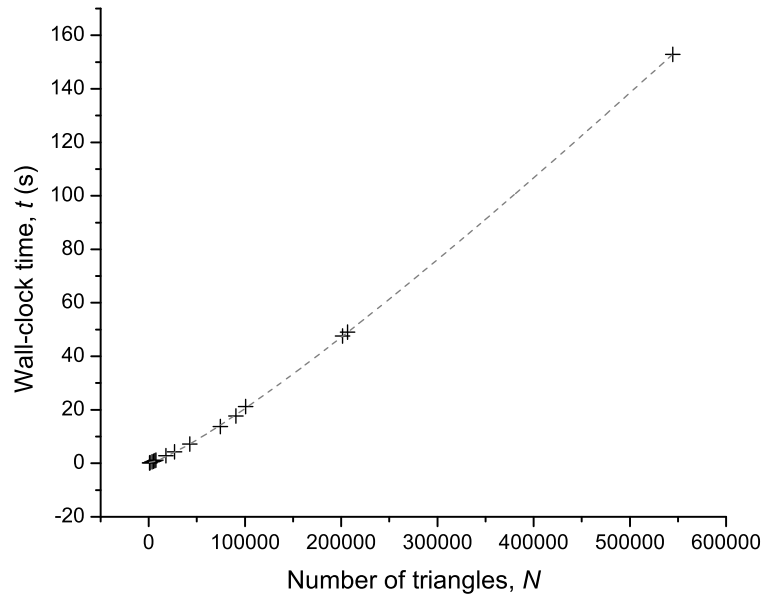


Figure 5: Wall-clock times of the horizon-shadow algorithm run for mesh sizes from 851 to 544507 triangles. The grey dashed line is a line of best fit of the form  $t = a_0 + a_1N + a_2(N \log N)$ . Wall-clock times are for one model timestep Feb 1, 2011 at 16:30, a time for which there are many triangles in shadow.

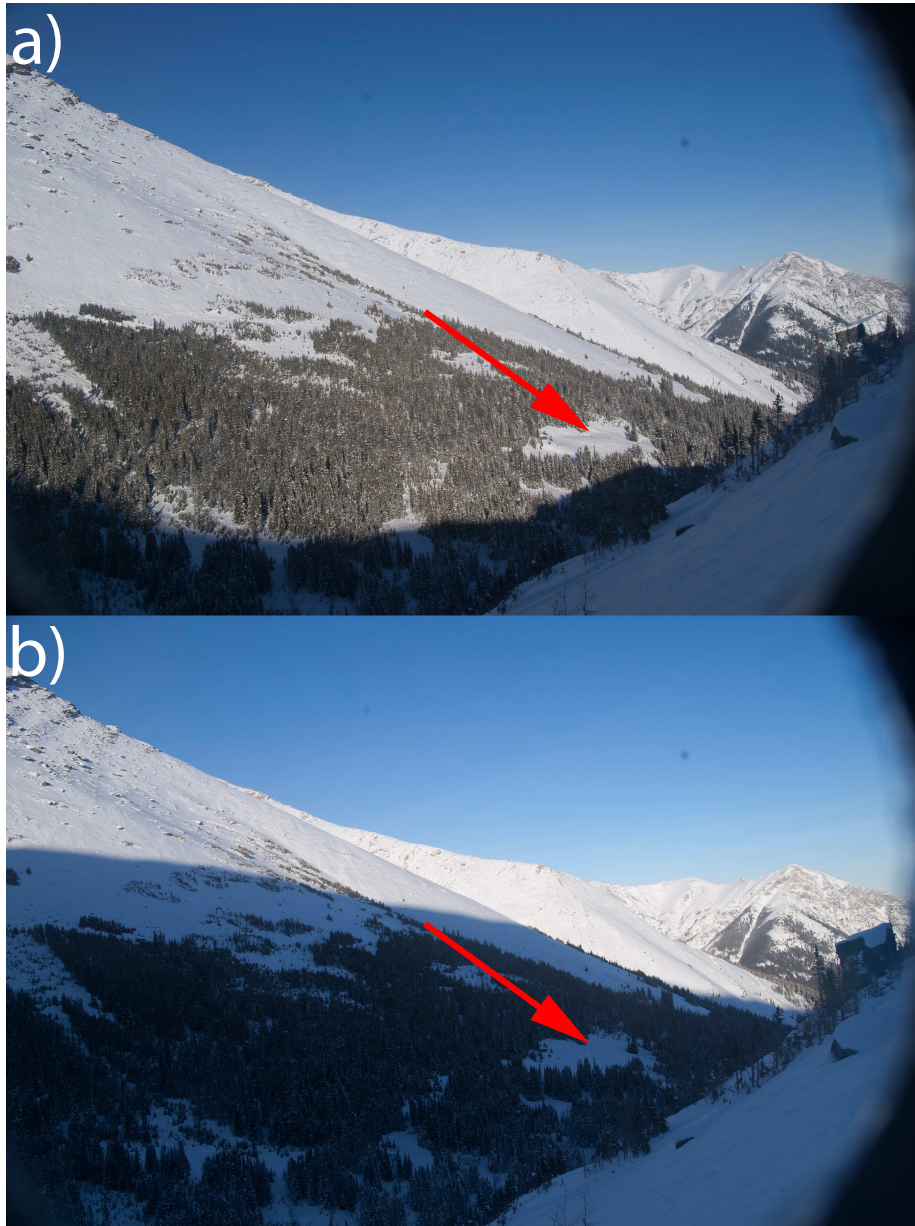


Figure 6: Time-lapse photographs from Fisera Ridge North showing shadow movement across the South Meadow site (red arrows). Photos taken Feb 1, 2011 at 16:00 (local) (a) and 17:00 (local) (b). Photos taken in an approximately eastward direction.

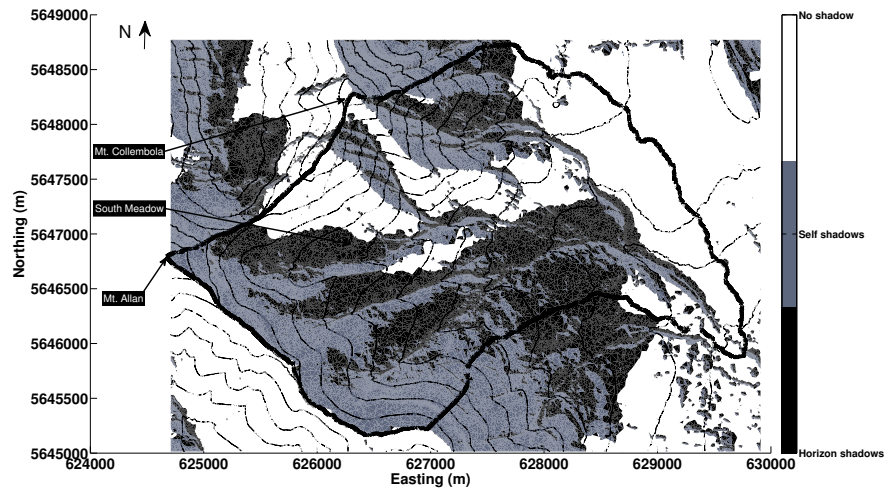


Figure 7: Marmot Creek Research Basin with modelled horizon and self-shadows. Areas in black, grey, and white are the horizon-, self-, and non-shadowed areas respectively. Model time: Feb 1, 2011 at 16:30. Contours are every 100 m, and the South Meadow site is indicated. This shows the horizon-shadow passing over the South Meadow site, something that is missed with only self-shadows.

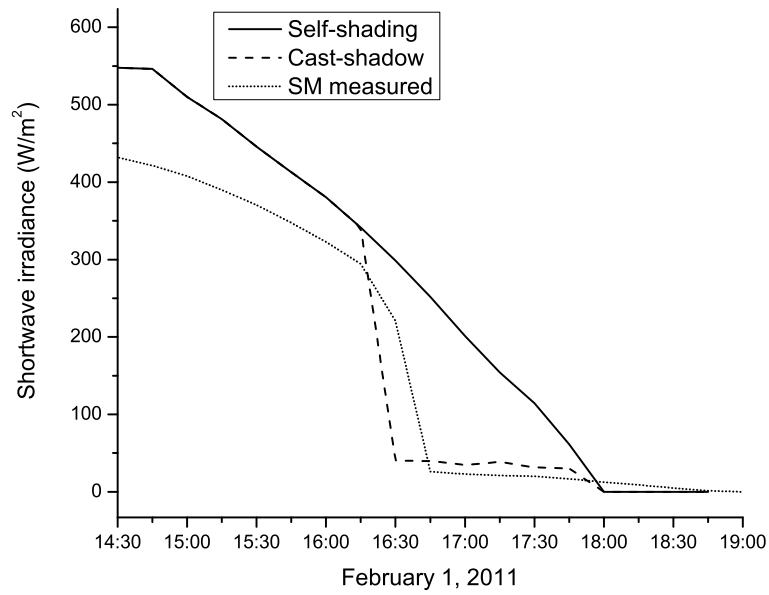


Figure 8: Shortwave irradiance for the clear-sky day February 1, 2011 at South Meadow. The solid line is the modelled irradiance using only a self-shading algorithm and diffuse beam, the dashed line is the modelled irradiance using the horizon-shadow algorithm and diffuse beam, and the fine dotted line is the measured irradiance (direct and diffuse beam). Because different instruments were used for South Meadow and the synthetic input data for the model, different amounts of reflected irradiance are present, as well as differences in the actual instruments resulting in the difference between measured and modelled.

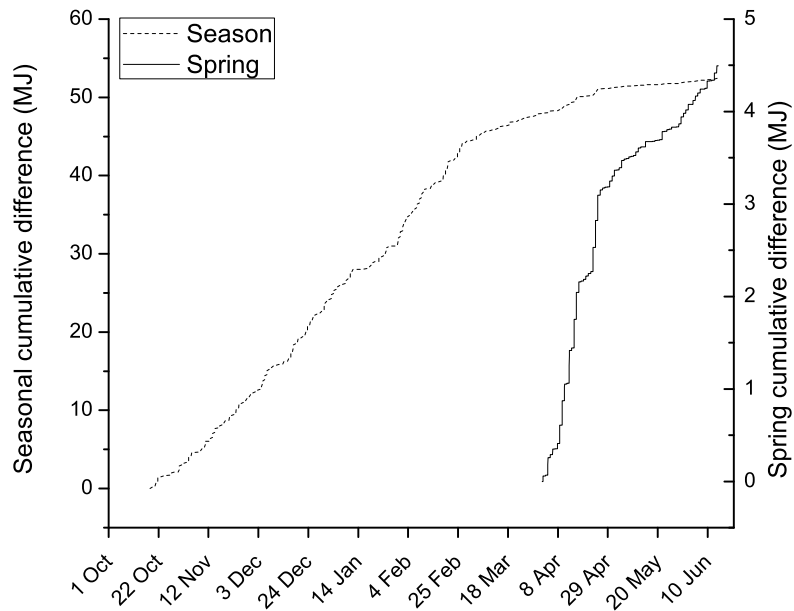


Figure 9: Cumulative difference in modelled shortwave irradiance between simulations using self-shading and horizon-shading algorithms at the South Meadow site for the season (October 17, 2010 to June 14, 2011) in the dashed line and for the spring (April 1, 2010 and Jun 14, 2011) in the solid line. An albedo of 0.8 is assumed.

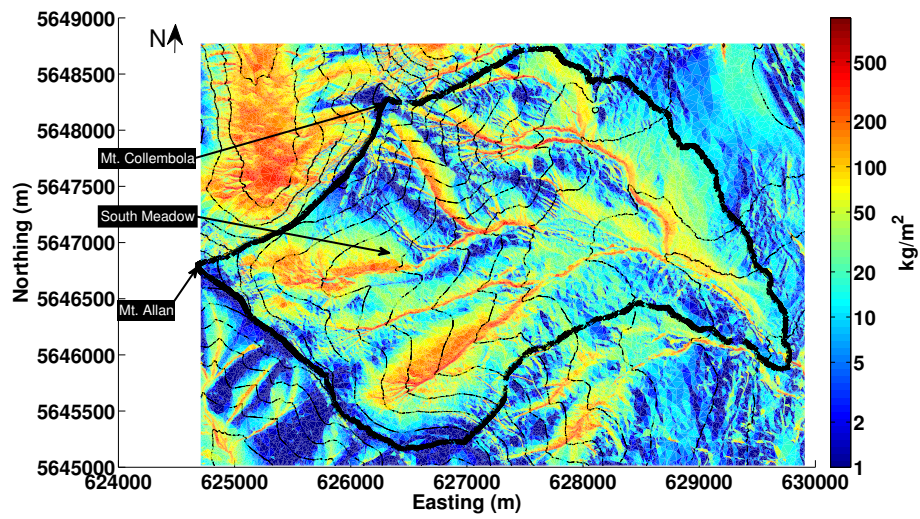


Figure 10: Cumulative seasonal difference (between October 17, 2010 and June 14, 2011) in simulations using self-shading and horizon-shading algorithms expressed as potential mass of melted snow. An albedo of 0.8 is assumed. Note the logarithmic scale. The Marmot Creek Research Basin is outlined in black and contour lines are every 100 m of elevation.

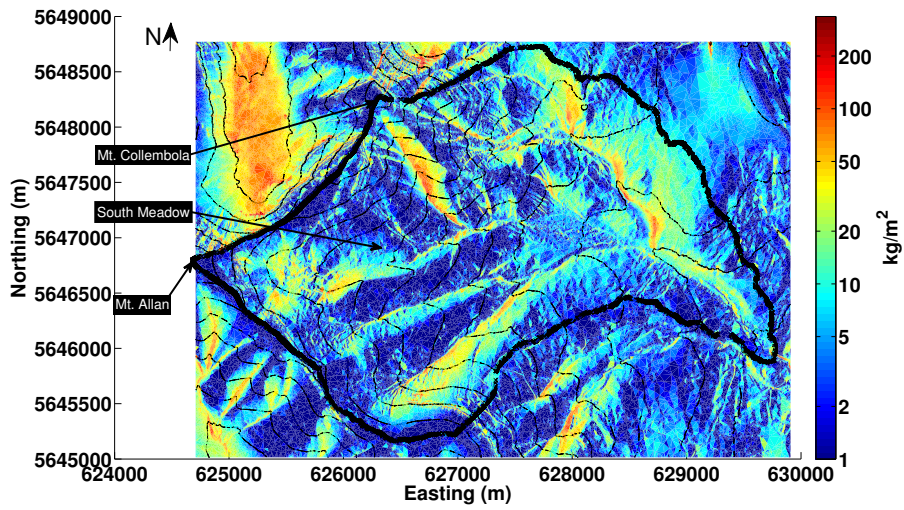


Figure 11: Cumulative seasonal difference (between April 1 and Jun 14, 2011) in simulations using self-shading and horizon-shading algorithms expressed as potential mass of melted snow. An albedo of 0.8 is assumed. Note the logarithmic scale. The Marmot Creek Research Basin is outlined in black and contour lines are every 100 m of elevation.